Draft version July 29, 2018
Preprint typeset using LaTeX style emulateapj v. 12/16/11

STAR FORMATION IN THE CENTER OF SPIRAL GALAXY NGC 4736

Farhanul Hasan[1], Alison Crocker[1]
[1] Department of Physics, Reed College, Portland, OR 97202
(Dated: Sept. 2017)
Draft version July 29, 2018

ABSTRACT

We estimate the star formation properties of the center and circumnuclear ring of spiral galaxy NGC 4736 (M94) using its population of observed young star clusters. We use *Hubble Space Telescope (HST)* observations to identify clusters in the center and the ring. We compare the observed photometry of the sources in our cluster catalog to those predicted by stellar evolutionary models to estimate masses, M, ages, τ, and extinctions, A_V, for each. We observe the mass function of clusters in the ring and center to both be well-approximated by a power law function, $dN/d\log M \propto M^{\beta}$ with β ∼-1.8. We use masses extrapolated from these mass functions to estimate the star formation rates (SFR) in a 100 Myr timescale. We find the surface density of star formation, Σ_{SFR} to be about 7 times as high in the ring as in the center, despite very similar surface gas densities, Σ_{gas}.

Subject headings: galaxies: individual: NGC 4736 – galaxies: starburst – galaxies: star clusters: general – stars: formation

1. INTRODUCTION

The currently accepted view of star formation is that most, if not all, stars form in clustered environments (e.g., Lada & Lada 2003; McKee & Ostriker 2007; Portegies Zwart et al. 2010). Clusters are formed in dense regions in giant molecular clouds (GMCs) by global hierarchical collapse (Vázquez-Semadeni et al. 2017). A variety of physical processes such as residual gas expulsion by massive young stars ("feedback") and tidal disturbances by passing molecular clouds cause these clusters to disrupt after some time, expelling the individual stars to the general field population. In young star clusters that are gravitationally bound, we assume that virtually all the stars are born at the same time and under very similar conditions (see Moraux 2016). Thus, they are ideal laboratories for studying the properties of stellar populations in galaxies and constraining theories of stellar evolution.

But how do stars form in the first place? Though we're far from a complete theory of star formation, it is widely accepted that the key ingredient for this process is the availability of cold gas. In particular, Kennicutt (1998) related the rate at which cold gas is converted to stars - the star formation rate (SFR) - to the cold gas available in the so-called Kennicutt-Schmidt relation:

$$\Sigma_{SFR} \propto \Sigma_{gas}^{N} \tag{1}$$

where Σ_{SFR} is the surface density of star formation (or SFR per unit surface area; often in units of $M_{\odot}$ yr^{-1} kpc^{-2}) and Σ_{gas} is the surface density of cold gas (in units of $M_{\odot}$ kpc^{-2}). The exponent, N, was established as 1.4 empirically. This relation has been seen to hold for entire galaxies and certain spatially resolved regions within a wide array of spiral and starburst galaxies.

However, star formation with efficiency lower than that predicted by (1) has been seen in early-type galaxies such as ellipticals and lenticulars (Crocker et al. 2012) and perhaps more surprisingly, the center of our own Milky Way, a spiral galaxy (Kauffmann et al. 2017). These observations indicate that gas density isn't the only determining factor, and that a complete theory of star formation must take into account the gravitational potential of gas, stars and the central supermassive black hole (SMBH), as well as negative feedback from supernovae winds which can eject cold gas from the center and other regions. A recent dynamical model by Krumholz et al. (2017) attempts to combine all of these elements into a comprehensive picture of star formation in galactic centers. NGC 4736 (a.k.a M94) is a spiral galaxy like our own but it lacks a strong nuclear bar, so it would provide a good test of the model with different physical properties than the Milky Way center.

In this work, we identify young star clusters in the center and ring of NGC 4736 and use their observed brightnesses to quantify the star formation efficiency (SFE; defined as the percentage of cold gas converted to stars in a given timescale) in both these regions. We compare the Kennicutt-Schmidt relation for the center and the ring and later will apply the dynamical model of Krumholz et al. (2017) to NGC 4736 and compare its predictions to the evidence for ongoing and/or past bursts of star formation in its center. We organize our paper as follows: section 2 presents the *Hubble Space Telescope (HST)* observations and describes our procedure for source detection and cluster selection, including the criteria for separating stars from clusters. In section 3, we derive the ages, masses, and extinction of light from all of our clusters by comparing the observed magnitudes to those predicted by Bruzual & Charlot's (2003) stellar evolution models. Section 4 presents the star formation estimates, including SFR and SFE (star formation efficiency) for the ring and center of the galaxy, which we compare to the Kennicutt-Schmidt predictions. We summarize our results and steps moving forward in section 5.

2. OBSERVATIONS AND CLUSTER CATALOGS OF NGC 4736

2.1. *Data*

The center and ring of NGC 4736 was imaged with the *Hubble Space Telescope's (HST)* Wide Field Planetary Camera 2 (WFPC2) in F336W and F555W ("U" and "V"; GO-10402, PI: R. Chandar), in F450W and F814W ("B" and "I"; GO-9042, PI: S. Smartt) and F656N ("Hα"; GO-8591, PI: D. Richstone). Data were obtained from the Hubble Legacy Archive. The pixel scale for these images is 0.″1 pix^{-1} or 2.2 pc pix^{-1} at NGC 4736's distance of ∼4.6 Mpc (distance modulus = 28.31; Tully et al. 2013). We show an RGB image of the galaxy in Fig. 1.

2.2. *Source detection and photometry*

For detecting point-like and extended sources in the center and ring of NGC 4736, we use the DAOStarFinder task (which uses the DAOFIND algorithm: Stetson 1987) in *photutils*, an affiliated package of *astropy* (Bradley et al. 2016). We run DAOStarFinder on our background-subtracted U, B, V, Hα, and I images, so that sources would be detected above the 5σ threshold. We match all sources detected in the U, B and V bands and then combined them with sources matched in at least one of the Hα and I bands. Our source catalog thus contained objects detected in at least 4 photometric bands. We then perform circular aperture photometry for all of our sources on all of our images using the DAOPHOT task *phot* (1987). For photometry, we use an aperture radius of 2.5 pix (corresponding to ∼5.5 pc in physical size) and subtract background light in an annulus of inner radius 10 pix and outer radius 12 pix for each source. The aperture corrections we make are described in the section below.

2.3. *Aperture corrections*

Given that each arcsecond imaged is equivalent to 10 pix, we needed to account for the light in the extended wings of the source that falls outside the aperture within which photometry is performed. To do this, we obtain aperture corrections using two different methods. Both methods use the difference in magnitude measured within a 10 and 2.5 pix aperture and an additional -0.1 mag addition to account for light from 1″ to infinity. The first is a fixed correction based on photometry of 30 relatively isolated, high S/N star clusters. To these, we apply an average -0.68 mag correction to the measured V-band magnitude. This approach systematically overestimates the total luminosity of more compact clusters and underestimates that of more extended ones.

For the second method, we correlate size (as diagnosed by full width at half maximum; FWHM) with aperture correction by generating artificial clusters of different sizes (see for example, Mora et al. 2007). We note that the the Point Spread Function (PSF) - which describes the two-dimensional distribution of light in the focal plane of a telescope for point sources - differs for each photometric band. Accordingly, the correction to aperture magnitude from photometry will also differ for each band. We use the *mksynth* task in BAOLAB to create synthetic images of star clusters of m$_V$ ∼20 and the *mkcmppsf* task to convolve a PSF for each band with a King (1966) profile of different FWHMs (in order to vary the sizes of artificial clusters). After performing photometry on these sources, we observe a linear best-fit relation between aperture correction, Δm, and FWHM. The relations were more or less identical for the five different bands, with slight offsets due to differences in how extended the PSFs are. We found this approach to be a much more reasonable way to correct for aperture photometry than applying a single mean correction for all sources.

2.4. *Sizes*

We obtain two different estimates of size for our sources. First, we measure the concentration index (CI), defined as the difference in V-band magnitude measured within a 3 and 0.5 pix radius, by performing photometry within those radii on our V-band image. The CI, besides being a decent measure of how extended an object is, provides a good diagnostic tool for separating individual stars from star clusters as stars appear unresolved even with very high resolution HST images. Thus, CI values are on average smaller and they vary little, with the distribution being peaked around an average value close to a stellar point spread function (PSF), while clusters, being more resolved, boast larger and more dispersed CIs (Grasha et al. 2015).

We also obtain the FWHM along the major axis for our sources, using the *ishape* task in BAOLAB (Larsen 1999). *ishape* models a source as an analytical function convolved with the PSF and then finds a best fit to the FWHM for each source, i.e. determines how much broader it is than the PSF. We create a PSF for the V-band image that is 10 times the resolution of the HST/WFPC2 PSF and assume a King (1966) profile with a ratio, r_{tidal}/r_{core}, of 30 and run *ishape* so that the FWHM of our sources is measured based on the flux in a 5 pix fitting radius (∼ 11 pc at the distance of NGC 4736). Since the FWHM returned by *ishape* is not a very reliable measure of sizes for sources with signal-to-noise (S/N) $\lesssim$30 and in crowded regions, we use both CI and FWHM in cluster selection criteria, as described in section 2.5.

2.5. *Cluster selection*

Similar to the approach in most recent works (e.g., Chandar et al. 2010; Whitmore et al. 2010; Chandar et al. 2016), we construct "training sets" of stars and clusters to guide our process of separating stars from clusters and creating a catalog of young clusters. We first hand-pick a set of point-like sources, i.e. stars, and a set of extended objects, i.e. clusters. Then we use their measured properties such as apparent V-band magnitude, m_V, concentration index, CI, and FWHM, to help us assign criteria to select young star clusters. Based on our training set (see Fig. 2), we use the following criteria to determine cluster candidates in NGC 4736:

1. $m_V \lesssim 22.5$ (i.e. $M_V \lesssim$ -5.8). Low-luminosity clusters are often dominated by a few bright stars, so this magnitude cut helps us secure more reliable size measurements. Around 5% of our matched sources were removed with this criteria.

2. 1.6 ⩽ CI ⩽ 2.8. As mentioned above, stars have smaller CI values which are much less dispersed than cluster CIs. We note that most of the objects with CI $\gtrsim$ 2.8 are likely faint stars with very bright companions nearby.

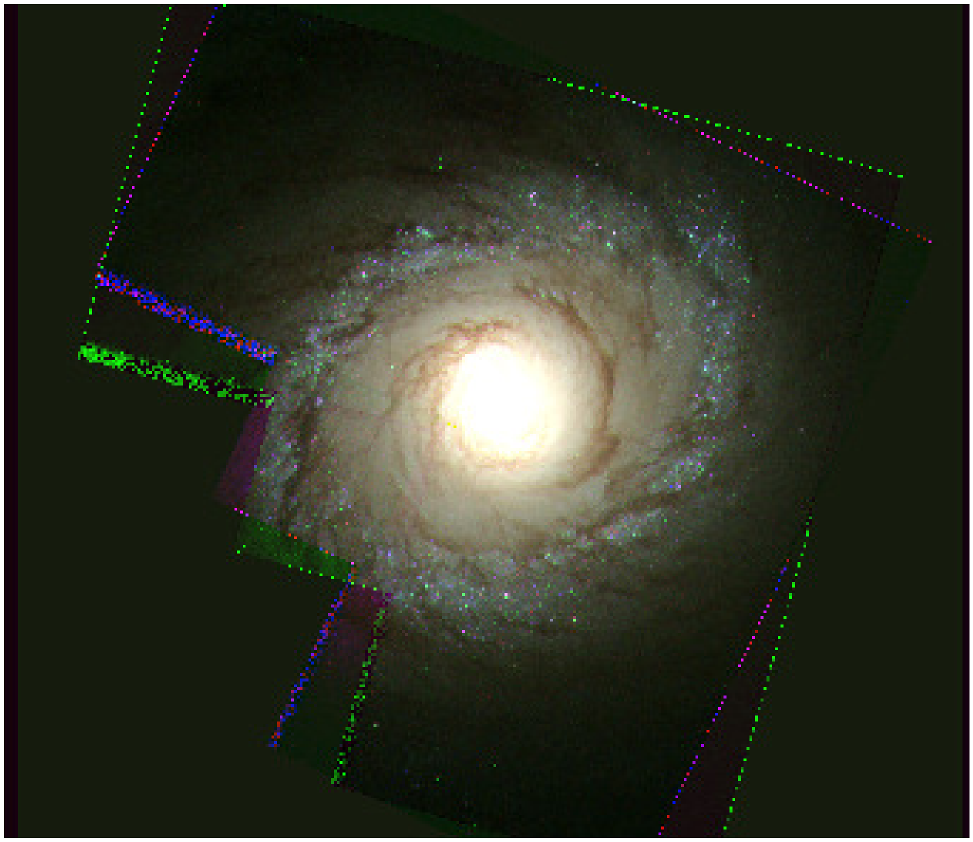

FIG. 1.— RGB image of NGC 4736. The blue band was mapped on to the U (F336W) filter, green to B (F450W), and red to I (F814W).

3. 0.15 pix $\leqslant$ FWHM $\leqslant$ 5 pix. (2) and (3) helped us select those objects which were extended enough to qualify as clusters, filtering out about 45% of the matched sources from our catalog.

4. Remove objects that satisfy (1) and (2) but have another source in a 2 pix (4.4 pc) radius around it. This helped us remove a few sources that are actually close pairs of stars that made the brightness and size cuts.

To test the completeness of our sample, we create artificial clusters using the *mkcmppsf* and *mksynth* tasks as above, and add them to our image which we then run the DAOFIND algorithm on. The fraction of sources recovered by DAOFIND helps us determine how complete our cluster catalog is at different brightness levels. We find that our sample is ≈90% complete at $m_V \sim 22.5$ mag across NGC 4736, with the level of completeness virtually equivalent for the nuclear region and the ring. The completeness level drops quicker for the ring than at the center (e.g. at $m_V = 23$ mag, the central region is ∼60% complete, while the annular region is ∼45% complete), which we infer to be an effect of crowding in the ring. Our final catalog contains **881** candidates for young stellar clusters in NGC 4736.

3. ESTIMATING AGE AND MASS OF CLUSTERS

3.1. *Fitting to stellar evolutionary models*

To determine the SFR in different regions of NGC 4736, we first require the ages and masses of our cluster

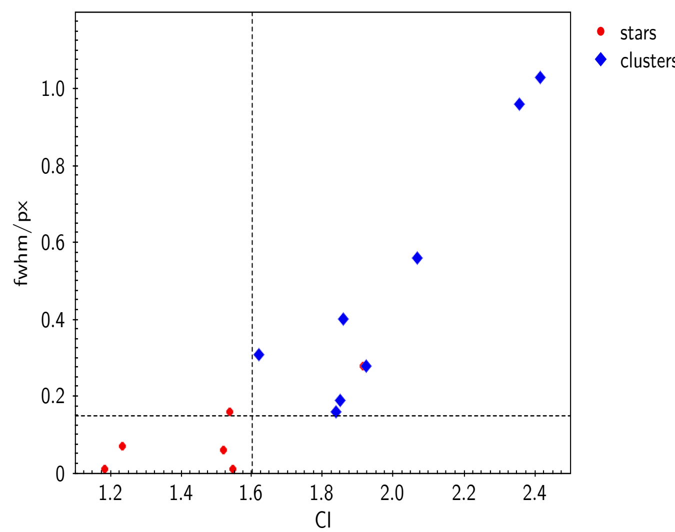

FIG. 2.— Training set values of FWHM and CI, used to guide our cluster selection criteria. The minimum cutoff for FWHM and CI are 0.15 pix and 1.6, respectively, and are shown as dashed lines.

candidates. We estimate age, τ, and extinction, A_V, for each cluster by performing a χ^2 fit of our observed magnitudes to those predicted by Bruzual & Charlot's (2003) stellar population synthesis models, assuming solar ($Z = 0.02$) metallicity, a Chabrier (2003) initial mass function (IMF), and a Galactic-type extinction law (Fitzpatrick 1999). The best-fit values of τ and A_V to the Bruzual & Charlot models minimize the statistic:

$$\chi^2(\tau, A_V) = \sum_\lambda W_\lambda (m_\lambda^{obs} - m_\lambda^{mod}(\tau, A_V))^2, \quad (2)$$

where m_λ^{obs} and m_λ^{mod} are the observed and model magnitudes, respectively, for a band with wavelength, λ. W_λ denotes the weight factor in each band, given by $W_\lambda = [\sigma_\lambda^2 + (0.05)^2]^{-1}$, where σ_λ is the uncertainty in the photometric measurement by DAOPHOT for each band. The sum runs over at least four, and in the case of about 70% of our sources, all five of the U,B,V,Hα and I bands. We obtain models for ages between 10^5 yr and 10 Gyr for clusters of initial mass 1 M$_\odot$. We first perform a minimization routine to obtain the best additive offset for each model at each extinction so that its magnitudes are scaled to appropriate masses for our sources. Given the mass-to-light ratios predicted by the models and assuming $\Delta(m-M) = 28.31$ (Tully et al. 2013) as before[1], we use these offsets to estimate the masses of our clusters. Then, we use our properly scaled models to find τ and A_V from the best fit models to each of our sources.

3.2. *Distribution of mass, age, and extinction*

In Fig. 3, we show the best-fit masses, M, and ages, τ, and extinctions, A_V, of all the clusters in our sample. Fig. 4 shows the distributions for the central and the circumnuclear ring regions separately. We note that there's no clear difference between the mass-age-extinction diagrams between the two regions. In both of these diagrams, the solid lines, for each extinction magnitude specified, correspond to the luminosity limit of 22.5 mags in the V-band, which we imposed as our criteria (1) during cluster selection (see section 2.5). Small-scale features in the $M-\tau$ diagram include the pile-up of clusters around $\log(\tau/\mathrm{yr}) \sim 6.5$ and ~ 7 and a lack of clusters in the $\sim 7 < \log(\tau/\mathrm{yr}) < \sim 7.5$ region. The latter, for example, occurs where the predicted colors loop back on themselves, covering a small region in color space over a relatively long time, and effectively resulting in a gap. These features are artifacts of the age-fitting procedure and do not affect the broad distribution of cluster ages and masses. We observed 71 young (τ <100 Myr) clusters in the center region (Fig. 5) of NGC 4736 with a total mass of $\sim 4 \times 10^5$ $M_\odot$, and 557 in the ring with total mass $\sim 3.6 \times 10^6 M_\odot$.

3.3. *Mass Functions*

The cluster mass function (CMF) provides important clues about the dynamical evolution of star clusters. The shape of the CMF provides strong constraints on physical properties, such as formation, disruption, and evolution of star clusters (e.g., Lada & Lada 2003; Portegies Zwart et al. 2010; Fall & Chandar 2012). For our study, the mass function serves the crucial purpose of extrapolating the mass of all low-mass clusters which cannot be detected by the WFPC2 (whose instrumental magnitude limit is $M \sim 24.5$). This will be used in our final calculation of cluster and star formation estimates. We construct a CMF for the central and ring regions of NGC 4736 separately (see Fig. 5) in order to obtain SF estimates for each separately.

[1] Adopting a shorter (longer) distance to M94 reduces (increases) the derived cluster masses

We construct mass functions for young clusters in NGC 4736 by counting the number of clusters observed in mass bins of $\log M/M_\odot = 0.1$. We find that the observed mass function over our mass-age domain can be described by a power law, i.e. $dN/d\log M \propto M^\beta$, for both regions. As shown in Fig. 6, the slope of the power law, β, is very similar for both regions, and as expected, the CMF declines with increasing mass. In the ring, a break from the simple power law is observed at the higher mass end ($> 3 \times 10^4 M_\odot$). There is debate in the literature about the existence of a truncation of the CMF - while many authors don't observe any obvious bends at the high-mass end (e.g., Chandar et al. 2010; Whitmore et al. 2010; Fall & Chandar 2012), some have found evidence for a cut-off mass at the high end of the CMF (e.g., Adamo et al. 2015; Bastian et al. 2012). The latter group report an exponential decline modeled by a Schechter (1976) function of the form $dN/d\log M \propto M^\beta \exp(-M/M_c)$, with the characteristic truncation mass M_c in the range $10^5 - 10^6 M_\odot$, to describe the form of the CMF. A recent study by Johnson et al. (2017) found a Schetchter form of the CMF in Andromeda (M31) and concluded the earlier disruption of higher mass clusters can be explained by a direct correlation between M_c and Σ_{SFR}, the surface density of star formation rate.

The low mass limit corresponding to our 90% completeness limit of $m_V \sim 22.5$ was 5000 $M_\odot$ and accordingly, we estimated our CMFs to be valid beyond this mass. We extrapolate the CMF below this limit and estimate the mass of clusters below this limit. We find that about 2/5 of the total mass of young clusters was not visible to our camera. Recovering 42.1% of the total mass in the center and 38.5% in the ring, we end up estimating 9.53 $\times 10^5 M_\odot$ and 9.34 $\times 10^6 M_\odot$ total mass in clusters in the center and the ring, respectively.

4. STAR FORMATION ESTIMATES

The star formation rate (SFR) is the total mass of cold gas converted to stars in a given time, and is a valuable statistic of star formation activity in clusters, galaxies, etc. The first ingredient in our star formation calculation is the cluster formation rate (CFR), which we obtain by simply adding up the total mass of clusters in a given timescale (100 Myr) and dividing by that timescale.

4.1. *Cluster formation Efficiency*

The next step is to determine the cluster formation efficiency (CFE), defined as the fraction of all star formation that occurs in bound clusters. The CFE quantifies the fraction of stars dispersed by gas expulsion (i.e. "infant mortality"), the fraction born in unbound clusters (or associations), and the fraction that survives the "cruel cradle effect." Kruijssen (2012) unifies all these elements into a comprehensive theoretical framework by integrating all the local clustering and survival properties over the full density spectrum of the interstellar medium (ISM). He derives the CFE as a function of observable properties such as surface gas density, Σ_g, angular velocity, ω, and the Toomre (1964) Q-parameter, q, globally and locally for nearby spiral, starburst, and dwarf galaxies. We apply Kruijssen's CFE_IDL routine available online (`http://www.mpa-garching.mpg.de/cfe`; 2012) to obtain CFEs for the center and ring of NGC 4736. In order to use the routine, we procured information about

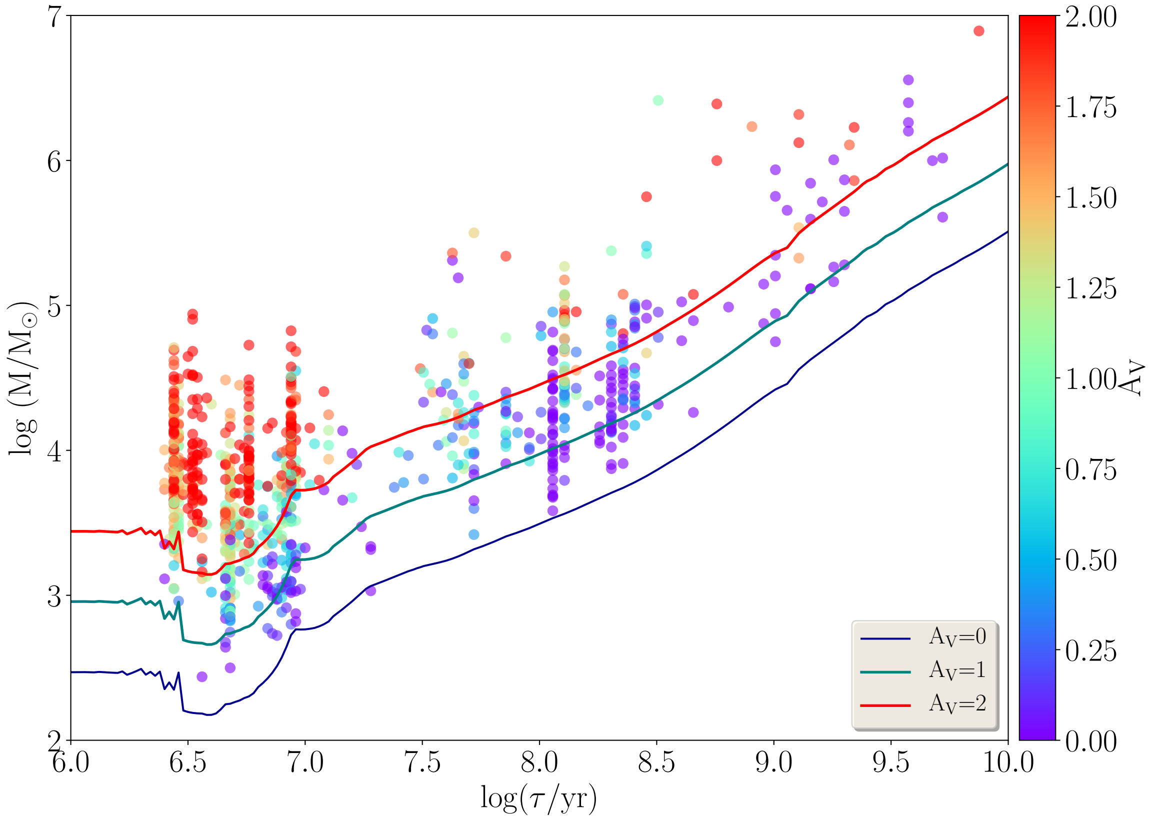

FIG. 3.— Observed masses, M, and ages, τ, of clusters in our sample, with extinctions, A_V, shown in color-coded auxiliary axis. The dark blue, teal, and red lines indicate the detection limits of A_V of 0, 1, and 2 mags respectively.

TABLE 1
DIFFERENCES IN STAR FORMATION EFFICIENCY BETWEEN INNER AND OUTER REGIONS

Quantity	inner region (center)	outer region (ring)
$\log \Sigma_g$ (M$_\odot$/pc^{-2})	1.07	1.12
Cluster formation rate (M$_\odot$/yr)	0.012	0.068
Cluster formation efficiency (%)	8.99	9.91
Star formation rate (M$_\odot$/yr)	0.107	0.951
$\log \Sigma_{SFR}$ (M$_\odot$ yr^{-1} kpc^{-2})	-1.19	-0.36
Star formation efficiency (%)	0.55	3.26

the dynamics of the galaxy from the literature. In particular, we used the rotation curve given by Buta (1988), the gas velocity dispersion, σ_g, from Kent (1987) and calculated the Toomre Q parameter for NGC 4736. The CFE_IDL routine calculated CFE of 8.99% for the center and 9.91% for the ring (see Table 1), and we find that these values differ by at most 1% with the upper and lower limits of the physical values of NGC 4736 we found from the literature.

4.2. *Kennicutt-Schmidt Law and star formation efficiency*

Using our values of CFE and CFR for the ring and center of NGC 4736, we proceeded to estimate SFR for the two regions. The surface density of SFR, Σ_{SFR} was found simply by applying the formula:

$$\Sigma_{SFR}(\mathrm{M_\odot yr^{-1} kpc^{-2}}) = \frac{(CFR/\Gamma)}{A} \quad (3)$$

where Γ is the CFE and A is the surface area, in kpc^2. We show in Table 1, that Σ_{SFR} in the ring is about 6.7 times as high as in the center.

The star formation efficiency (SFE) is the fraction of available cold gas used up in star formation. This is obtained from the slope of Fig. 7. We observe $\gtrsim 6$ times as efficient star formation in the ring than in the center. We believe the SFE would only decrease as we narrow in

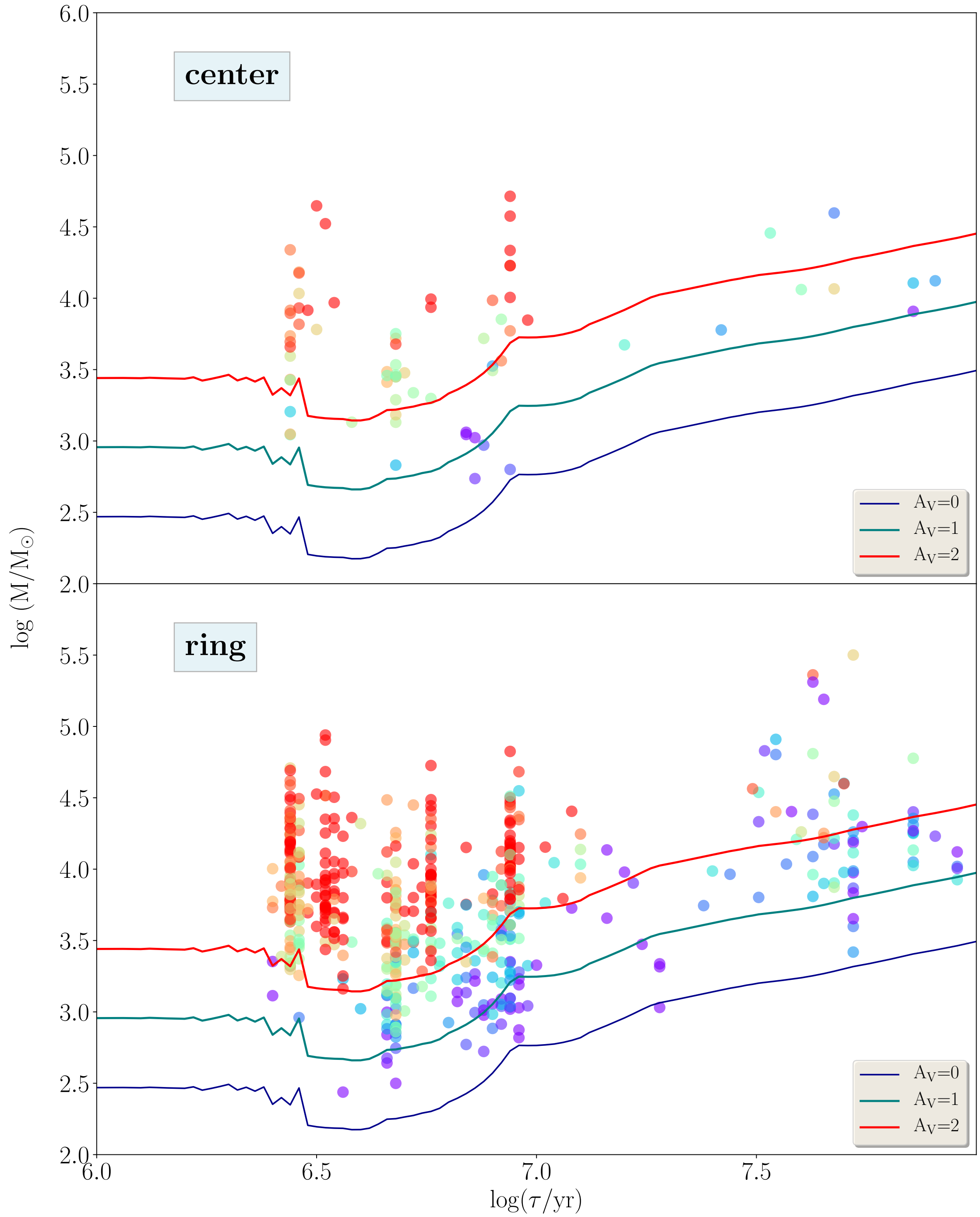

FIG. 4.— Observed masses, M, and ages,τ, and extinctions, A_V, of clusters in the center (upper panel) and ring (lower panel).

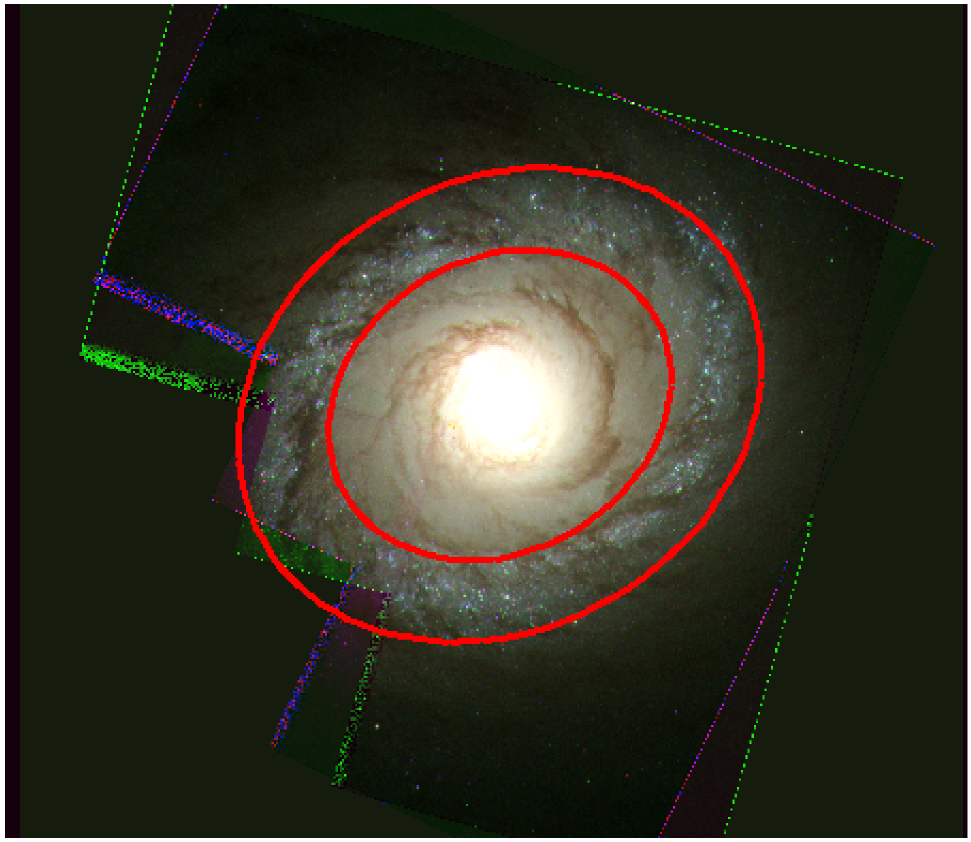

FIG. 5.— Central (inner ellipse) and ring (outer ellipse) regions of NGC 4736 identified.

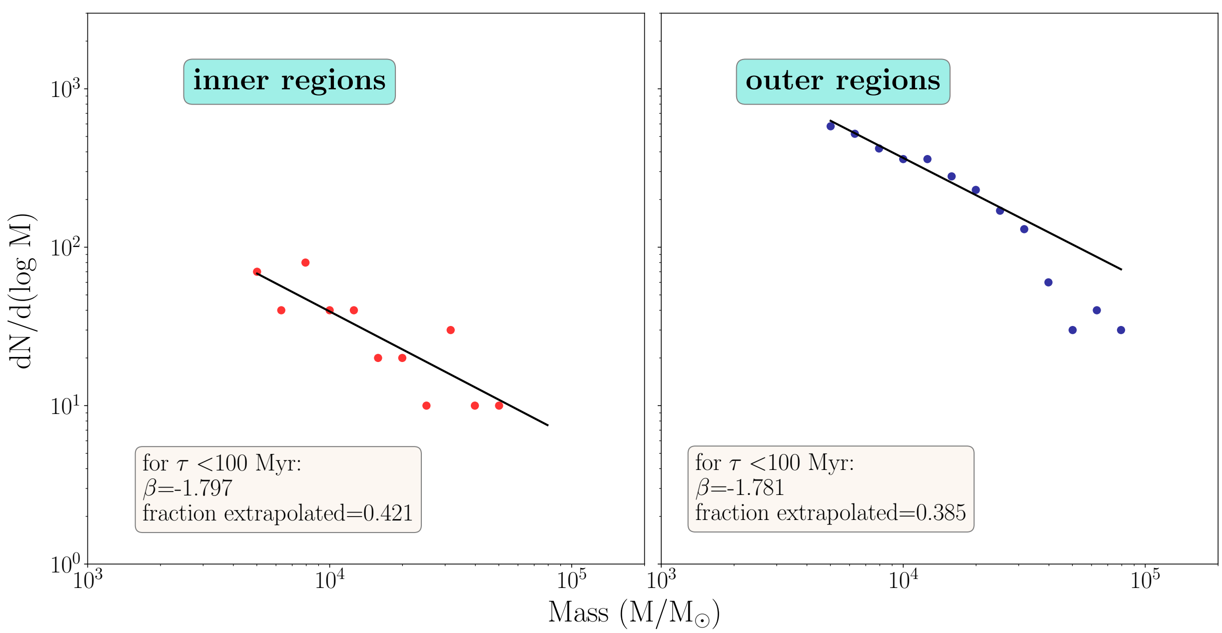

FIG. 6.— Cluster Mass function of young (τ < 100 Myr) star clusters in NGC 4736. The left panel shows the CMF of the central region, while the right panel shows CMF of the ring.

on the central regions, as our Σ_{gas} averages all the gas content in a larger ellipse and there is likely much greater density of gas available in, say the central 100 parsecs of the galaxy (for e.g., Barnes et al. (2017) found the inner few hundred parsecs of the Milky Way to harbor gas densities orders of magnitudes higher than the disc).

Fig. 7 shows where the center (yellow circle) and ring (purple triangle) of NGC 4736 lie in the Σ_{SFR}-Σ_g plane. Given Kennicutt's (1998) prediction of greater gas density inducing higher star formation, we would expect similar Σ_{SFR} for both regions since Σ_g is is very similar for both. This is clearly not the case we observe, leading us to the conclusion that we need more data points to assess the validity of the Kennicutt-Schmidt relation within all spatially resolved regions of NGC 4736.

5. SUMMARY AND MOVING FORWARD

We studied the star formation properties of the spiral galaxy NGC 4736. We used U, B, V, Hα and I images of NGC 4736 taken by the WFPC2 on board the *HST* to determine young, open clusters in the center and in the ring of the galaxy. We compiled a catalog of 881 young star cluster candidates. We compared our observed photometry to the magnitudes predicted by Bruzual & Charlot's (2003) stellar population synthesis models to obtain estimates of age, τ, Mass, M, and extinction, A_V, of these sources. Using the observed distribution of masses in intermediate and high-mass clusters, we calculated mass functions in the center and in the ring, and found them both to be well-estimated by a power-law function with slopes of ~-1.8 for both (albeit we did notice a break in the mass function for the ring at $M > 3\times10^4 M_\odot$). Using a (more) complete census of total cluster mass in both center and ring, we obtain cluster formation rate (CFR) in a 100 Myr timescale and use Kruijssen's (2012) analytical model to determine cluster formation efficiency, Γ. We then estimated the surface density of SFR for both regions of the galaxy and established that even though the gas surface density is fairly similar in both, Σ_{SFR} is about 7 times as high in the ring as in the center.

Moving forward, we hope to achieve the following:

- Rigorously assess the quality of our estimates of CFR, SFR and SFE by deriving statistical uncertainties in M, τ, and A_V from our χ^2 fitting procedure.

- Estimate the central rotation curve of the nuclear region of NGC 4736 by fitting the CO datacube (obtained from CO emission data) and then input it to the model of Krumholz et al. (2017). The different rotation curve and lack of a strong nuclear bar of this galaxy will give us a new test to this model, enabling us to confirm or deny the hypothesis that it's an adequate description of galactic centers and star formation therein of a galaxy different to ours.

- Compare the predictions of the Krumholz et al. (2017) model to the evidence for ongoing and/or previous episodes of star formation. One way to go about this would be to look at the observed age distribution of our clusters.
- Compare our SFRs derived from star clusters with those derived from typical SFR tracers such as UV and Hα emission. We expect these tracers to overestimate SFR.

We would like to thank Jim Borders and the Borders fellowship for supporting F.H. financially throughout the summer for this project.

REFERENCES

Adamo, A., Kruijssen, J. M. D., Bastian, N., Silva-Villa, E., & Ryon, J. 2015, MNRAS, 452, 246

Barnes, A. T., Longmore, S. N., Battersby, C., et al. 2017, MNRAS, 469, 2263

Bastian, N., Konstantopoulos, I. S., Trancho, G., et al. 2012, A&A, 541, A25

Bradley, L., Sipocz, B., Robitaille, T., et al. 2016, Photutils: Photometry tools, Astrophysics Source Code Library, ascl:1609.011

Bruzual, G., & Charlot, S. 2003, MNRAS, 344, 1000

Buta, R. 1988, ApJS, 66, 233

Chabrier, G. 2003, PASP, 115, 763

Chandar, R., Whitmore, B. C., Dinino, D., et al. 2016, ApJ, 824, 71

Chandar, R., Whitmore, B. C., & Fall, S. M. 2010, ApJ, 713, 1343

Chandar, R., Whitmore, B. C., Kim, H., et al. 2010, ApJ, 719, 966

Crocker, A., Krips, M., Bureau, M., et al. 2012, MNRAS, 421, 1298

Fall, S. M., & Chandar, R. 2012, ApJ, 752, 96

Fitzpatrick, E. L. 1999, PASP, 111, 63

Grasha, K., Calzetti, D., Adamo, A., et al. 2015, ApJ, 815, 93

Johnson, L. C., Seth, A. C., Dalcanton, J. J., et al. 2017, ApJ, 839, 78

Kauffmann, J., Pillai, T., Zhang, Q., et al. 2017, A&A, 603, A89

Kennicutt, Jr., R. C. 1998, ApJ, 498, 541

Kent, S. M. 1987, AJ, 93, 816

King, I. R. 1966, AJ, 71, 64

Kruijssen, J. M. D. 2012, MNRAS, 426, 3008

Krumholz, M. R., Kruijssen, J. M. D., & Crocker, R. M. 2017, MNRAS, 466, 1213

Lada, C. J., & Lada, E. A. 2003, ARA&A, 41, 57

Larsen, S. S. 1999, A&AS, 139, 393

McKee, C. F., & Ostriker, E. C. 2007, ARA&A, 45, 565

Mora, M. D., Larsen, S. S., & Kissler-Patig, M. 2007, A&A, 464, 495

Moraux, E. 2016, in EAS Publications Series, Vol. 80, EAS Publications Series, ed. E. Moraux, Y. Lebreton, & C. Charbonnel, 73–114

Portegies Zwart, S. F., McMillan, S. L. W., & Gieles, M. 2010, ARA&A, 48, 431

Schechter, P. 1976, ApJ, 203, 297

Stetson, P. B. 1987, PASP, 99, 191

Toomre, A. 1964, ApJ, 139, 1217

Tully, R. B., Courtois, H. M., Dolphin, A. E., et al. 2013, AJ, 146, 86

Vázquez-Semadeni, E., González-Samaniego, A., & Colín, P. 2017, MNRAS, 467, 1313

Whitmore, B. C., Chandar, R., Schweizer, F., et al. 2010, AJ, 140, 75

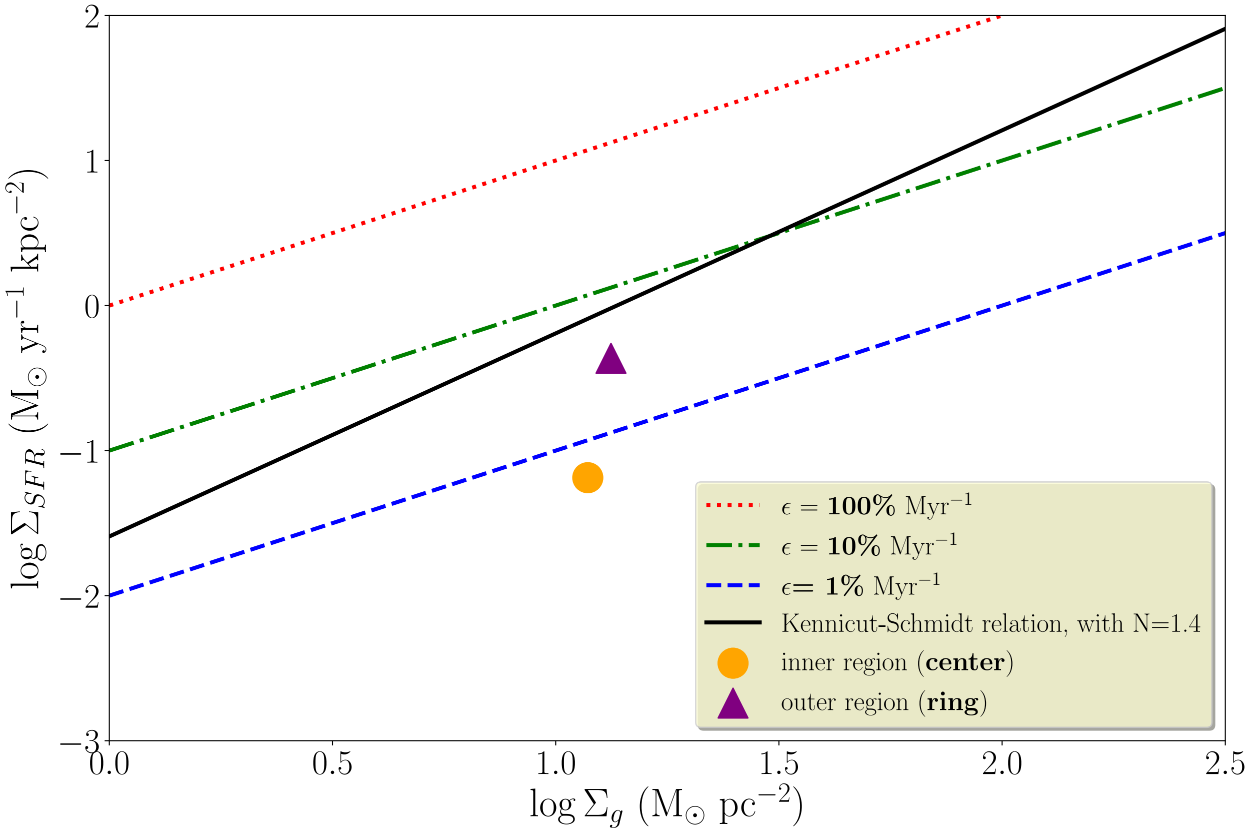

Fig. 7.— star formation rate surface density (Σ_{SFR}) compared to average gas surface density (Σ_g), with the Kennicutt-Schmidt (1998) relation for an empirically determined exponent of N=1.4. The red, blue and green dashed lines represent constant SFE of 100%, 10%, and 1%, respectively, in a 1 Myr timescale.